IEEE Access
Multidisciplinary ⋮ Rapid Review ⋮ Open Access Journal

Received November 3, 2018, accepted January 7, 2019, date of publication January 11, 2019, date of current version February 4, 2019.

Digital Object Identifier 10.1109/ACCESS.2019.2892231

Simulation and Experimental Verification of Edge Blurring Phenomenon in Microdefect Inspection Based on High-Frequency Ultrasound

LEI SU[1,2], XIAONAN YU[1], KE LI[1], XINGYAN YAO[3], AND MICHAEL PECHT[4], (Fellow, IEEE)
[1]Jiangsu Key Laboratory of Advanced Food Manufacturing Equipment and Technology, Jiangnan University, Wuxi 214122, China
[2]State Key Laboratory of Digital Manufacturing Equipment and Technology, Huazhong University of Science and Technology, Wuhan 430074, China
[3]Chongqing Engineering Laboratory for Detection Control and Integrated System, Chongqing Technology and Business University, Chongqing 400067, China
[4]Center for Advanced Life Cycle Engineering, University of Maryland, College Park, MD 20742, USA

Corresponding authors: Lei Su (lei_su2015@jiangnan.edu.cn) and Ke Li (like@jiangnan.edu.cn)

This work was supported in part by the National Natural Science Foundation of China under Grant 51705203, Grant 51775243, and Grant 51605061, in part by the Key Project of Industry Foresight and Common Key Technologies of Jiangsu Province under Grant BE2017002-2, in part by the Natural Science Foundation of Jiangsu Province under Grant BK20160183, in part by the project funded by the China Postdoctoral Science Foundation under Grant 2017M611690, in part by the Open Foundation of the State Key Laboratory of Digital Manufacturing Equipment Technology under Grant DMETKF2018022, and in part by the 111 Project under Grant B18027.

ABSTRACT Acoustic micro-imaging based on high-frequency ultrasound has been widely and effectively used for microdefect detection in microelectronic packages. With the miniaturization of microelectronic devices and the reduction of defects, edge blurring occurs in high-frequency ultrasonic scanning and directly affects the detection accuracy and signal-to-noise ratio, especially in spherical structures, such as ball grid arrays, wafer-level chip-scale packaging, and flip-chip solder bumps. This paper depicts the ultrasound interaction behaviors and the edge blurring effects during microdefect imaging, which provide a theoretical basis for improving the defect detection accuracy in subsequent research. A microdefect finite-element model was developed to simulate scanning in acoustic microscopy imaging. C-lines and C-scans of microdefects of various sizes were obtained, which can identify the location and size of the defects more easily. Furthermore, an improved method to obtain the acoustic propagation path map was developed for analyzing the acoustic energy transmission during detection. Different energy consumption paths around the microdefect lead to differences among the C-lines. The different sizes of microdefects show different blurred edges in the C-scans. The experimental data and simulation show consistent results, which prove the credibility of the developed method.

INDEX TERMS Microdefects, acoustic micro-imaging, edge blurring, acoustic propagation map.

I. INTRODUCTION

Defects in microelectronic packages have a serious influence on device reliability [1]–[3]. The common nondestructive evaluation methods for microdefect detection include X-ray [4]–[8], infrared thermography [9], [10], vibration analysis [11], [12], and acoustic micro-imaging (AMI) [13]–[15]. X-ray inspection technology is widely used in defect detection, but it requires expensive special equipment and an experienced operator. Lu *et al.* [10] established a flip-chip defect detection system based on active infrared detection technology to distinguish the temperature differences between a missing solder ball and a defect-free solder ball, and to diagnose and identify defects. Compared with infrared thermography technology, AMI has higher resolution, which can be up to submicron scale. AMI is a typical nondestructive testing method based on high-frequency ultrasound [16]. It avoids harmful radiation from X-rays and can pinpoint and visually display results compared to vibration analysis [17]. AMI has been widely applied for defect inspection of flip-chip solder bumps, such as missing solder balls, voids, and delamination [18], [19].

AMI uses a high-frequency focusing probe that emits a pulsed ultrasound wave, which is incident on the inside of the detection object through the acoustic lens and the coupling medium. The ultrasonic waves are reflected, refracted, and scattered at the internal interface. The echo signals are acquired again by the probe and processed by the signal processing system. The probe scans the entire detection area

2169-3536 © 2019 IEEE. Translations and content mining are permitted for academic research only.
Personal use is also permitted, but republication/redistribution requires IEEE permission.
See http://www.ieee.org/publications_standards/publications/rights/index.html for more information.

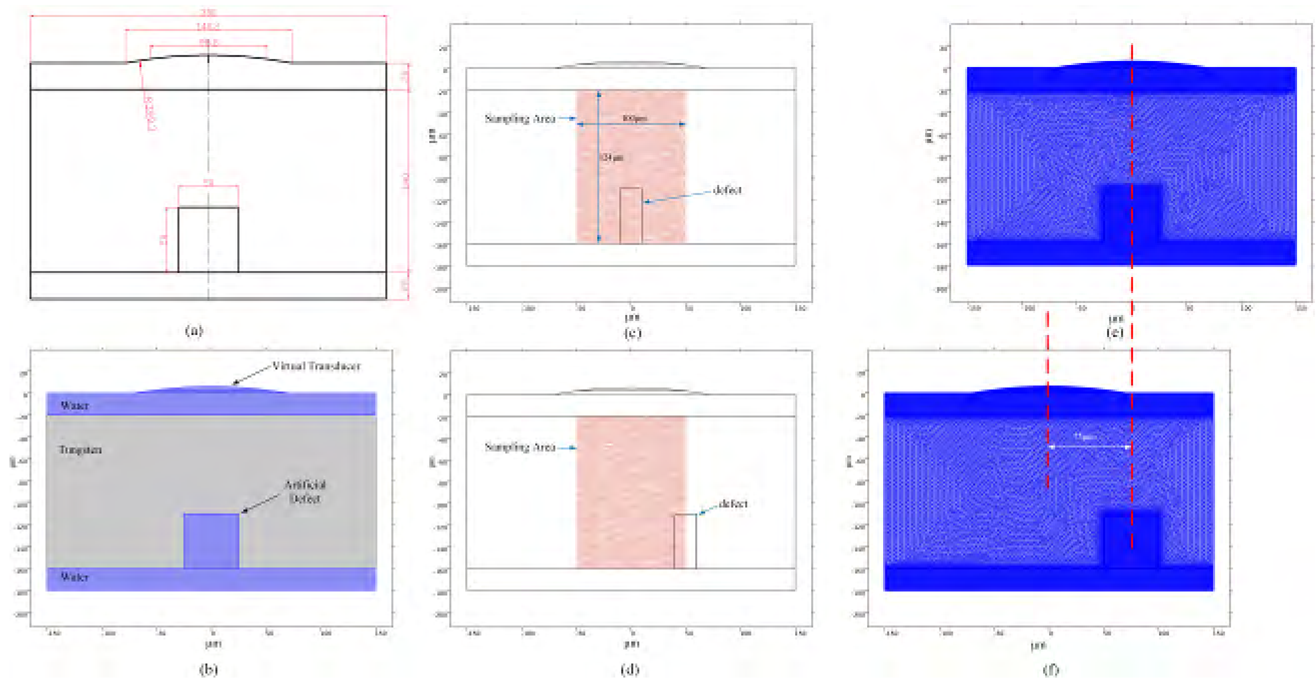

FIGURE 1. The simulation models including the microdefects with a height of 50 μm and a width ranging from 1 μm to 100 μm (unit in μm): (a) the simulation model (unit in μm); (b) area segments in the model; (c) ampling grid for calculating the acoustic propagation map; (d) the VT moves a distance of 50 μm to sampling; (e) meshing; and (f) the VT moves a distance of 75 μm to emulate the scanning in AMI.

in the scan plane to form a scanned image based on the single-point detection results. In the current ultrasonic inspection system, due to the fluctuation characteristics of ultrasonic waves, the focus of the transducer is not an ideal point but a region close to the wavelength scale, and the range of the focus depends on the shape and the frequency of the transducer. For the normally used 230 MHz transducer, the spot size can reach tens of microns. At the same time, the scanning step of the imaging system can be up to 1 μm or even smaller. The ultrasound will be scattered or refracted by the edge geometry of the defect, resulting in the blurring of the ultrasound image [14]. This blurring seriously affects the detection precision of micron-scale defects. As microelectronic devices trend to miniaturization [16], [20], the characteristics of high density and fine pitch of flip chips result in smaller-scale defects, and the edge effect becomes more significant [21]. Therefore, it is necessary to study the edge effect of microdefects in the AMI. Several investigations have focused on these phenomena. Ding *et al.* [22] identified the interaction behaviors between the focused ultrasound beam and the defect, which have a negative impact on the acoustic imaging process [23], whereas the explanation for the generation of the edge effect was lacking and the size of the object was up to millimeters. As the acoustic propagation around microdefects within the solid specimen cannot be measured directly, it is hard to explain the edge effect. Lee *et al.* [21] developed a finite element transient model for solder bumps to study the acoustic wave propagation inside the flip-chip package, but did not consider the edge effect leading to blurring.

In this paper, we develop finite element models to emulate the microdefect detection process by using COMSOL Multiphysics coupling software, and further calculated the acoustic propagation map for analyzing the acoustic energy transmission. According to the C-lines [21] and the C-scans together with the maps, we reveal the acoustic interaction behavior and clarify the edge blurring effect. The simulation results are verified by experiments.

II. SIMULATION

A. MODELING

With the limitation of computing capability and the feasibility of experimental verification, we chose tungsten for simulation and experiment based on the experimental conditions in our lab. The finite element models, as shown in Fig. 1(a), were developed with COMSOL Multiphysics 5.2 software. The 230 MHz probe (Sonoscan 230SP) used in the experiment has a focal length of 7924.8 μm in pure water. Since each wavelength was divided into 6–15 grids in the simulation, if the model was directly developed according to the actual size of the probe, the number of model grids would be tens of millions, which is not convenient for further data analysis. For simplifying computation, we scaled the real transducer to a virtual transducer (VT) according to the isometric scaling principle, with the size of 1/20 of the real transducer in the model. In the whole simulation model, the size of the medium water was the largest and the sound velocity in the medium water was the smallest, so the number of grids in the medium water occupied the largest part of the grids when they were divided according to the wavelength of

TABLE 1. Material properties in simulation.

Material	Sound Speed (m/s)	Density (Kg/m^3)	Poisson's Ratio	Young's Modulus (GPa)
Water	1484	1000	/	/
Tungsten	4620	17800	0.27	360

the sound wave. The propagation of the sound wave in the medium water was simplified to can minimize the distortion of simulation results and significantly reduce the number of grids. At the same time, the size of the solid region was also reduced and the microdefects were highlighted. Thus, the size of the model and the number of grids could be reduced, while the physical law of the interaction between acoustic waves and microdefects could be retained as far as possible. The model used a circular arc to simulate a virtual probe with an arc length of 98.8 μm and a radius of 399.3 μm. The thickness of the corresponding conductive medium water was also reduced to 20 μm, and the microdefects had a height of 50 μm with the width ranging from 1 μm to 100 μm, as shown in Figure 1(a). Deionized water was the coupling media. The detailed material properties were set using COMSOL's material library. The specific data are shown in Table 1. The solid/liquid interface was set as an acoustic-structural boundary, and the other boundaries were set as plane wave radiation boundaries in the liquid region and low-reflection boundaries in the solid region. The grid was set as 10 elements per wavelength. The simulation process included ultrasonic signal transmission and reception, a coupling medium (deionized water), and a measurement object. The ultrasonic signal was incident into the water by loading the normal displacement boundary condition on the incident arc. The loading signal was of the Gabor function type, and the signal length was about 10 ns. The specific expression is

$$f(t) = A \cdot \exp(-\frac{\pi(t-\mu)^2}{\sigma^2}) \cdot \sin(2\pi f_0 t) \tag{1}$$

where A is the reference amplitude, f_0 is the central frequency of the transducer (230 MHz), and $\mu = 2/f_0$ and $\sigma = 1/(2f_0)$ are the translation and standard deviation of Gaussian function, respectively.

The simulation process was performed in two steps. First, the probe loaded the excitation signal for 20 ns. The excitation signal was then removed and its boundary condition was modified to be the scattering boundary for 70 ns. The sound pressure integral of the arc where the probe was located was used as the receiving signal.

To emulate the scanning process of the AMI, the simulation was performed at the position of the microdefect when horizontally changing at 1 μm intervals. Finally, the VT was moved a distance of 75 μm, and the simulations were performed 76 times, as schematically shown in Figures 1(e) and 1(f).

To investigate the acoustic propagation during the microdefect detection, an improved method was developed to obtain the acoustic propagation map (APM) for better analyzing the acoustic energy transmission around the microdefect. This method can compress the sound propagation process in the entire time domain into a picture, so that the phenomena of transmission, emission, refraction, and diffraction during the sound propagation can be visually observed. The sampling area is shown in Figure 1(b). In the different probe detection positions, our adopted area was always under the probe, the sampling area was 100 μm wide and 124 μm high, and the space sampling interval was 1 μm. According to the size of the simulation model and the propagation speed of ultrasound, and in order to ensure that the interaction process between sound waves and microdefects can be completely extracted, we set the sampling time range to 20 ns to 50 ns, and took the data every 0.2 ns. In the sample area, the extracted transient solution is the displacement of the coordinate point, and in the liquid region, the extracted transient solution is the pressure at the coordinate point. The data of the displacement and pressure sampled from the transient times 26 ns (step 31), 32 ns (step 61), 38 ns (step 94), 42.6 ns (step 114), and 50 ns (step 151) together with the calculation flow diagram are shown in Figure 2. These data were inserted into two three-dimensional matrices which contain geometric and time information, one for the displacement data in the solid region and the other for the pressure data in the fluid region. Then, the squared value of the displacement data and absolute value of the pressure data were calculated, normalized, and combined into one joint matrix as a unified unit of energy. Here, the absolute value of the pressure data was adopted because the energy intensity in the liquid was linear with the pressure. Finally, we aggregated (Sum operation) and maximized (Max operation) the joint matrix along the time dimension, and obtained the acoustic energy flux map (AEFM) and acoustic energy peak path map (AEPPM) as

$$AEFM_{x,y} = \sum_{t} \left[disp^2, |p_t| \right]_{x,y,t} \tag{2}$$

$$AEPPM_{x,y} = \max_{t} \left[disp^2, |p_t| \right]_{x,y,t} \tag{3}$$

where $disp$ is the displacement data in the solid region, p_t is the pressure data in the fluid region, x and y are the geometry coordinates, and t is the transient time step. The AEFM displays the reflection behavior, and the AEPPM shows the path of the acoustic energy peak isolating direction and the magnitude of specific waves.

B. C-LINES AND C-SCANS

The normalized A-scan signal and C-line of the model are illustrated in Figure 3. Time domain signals were obtained by transient simulation, that is, a sweep signal also contains the initial VT excitation signal, known as the main bang mode as shown in Figure 3(a). Three pulses represent the initial excitation signal, the echo of the surface, and the

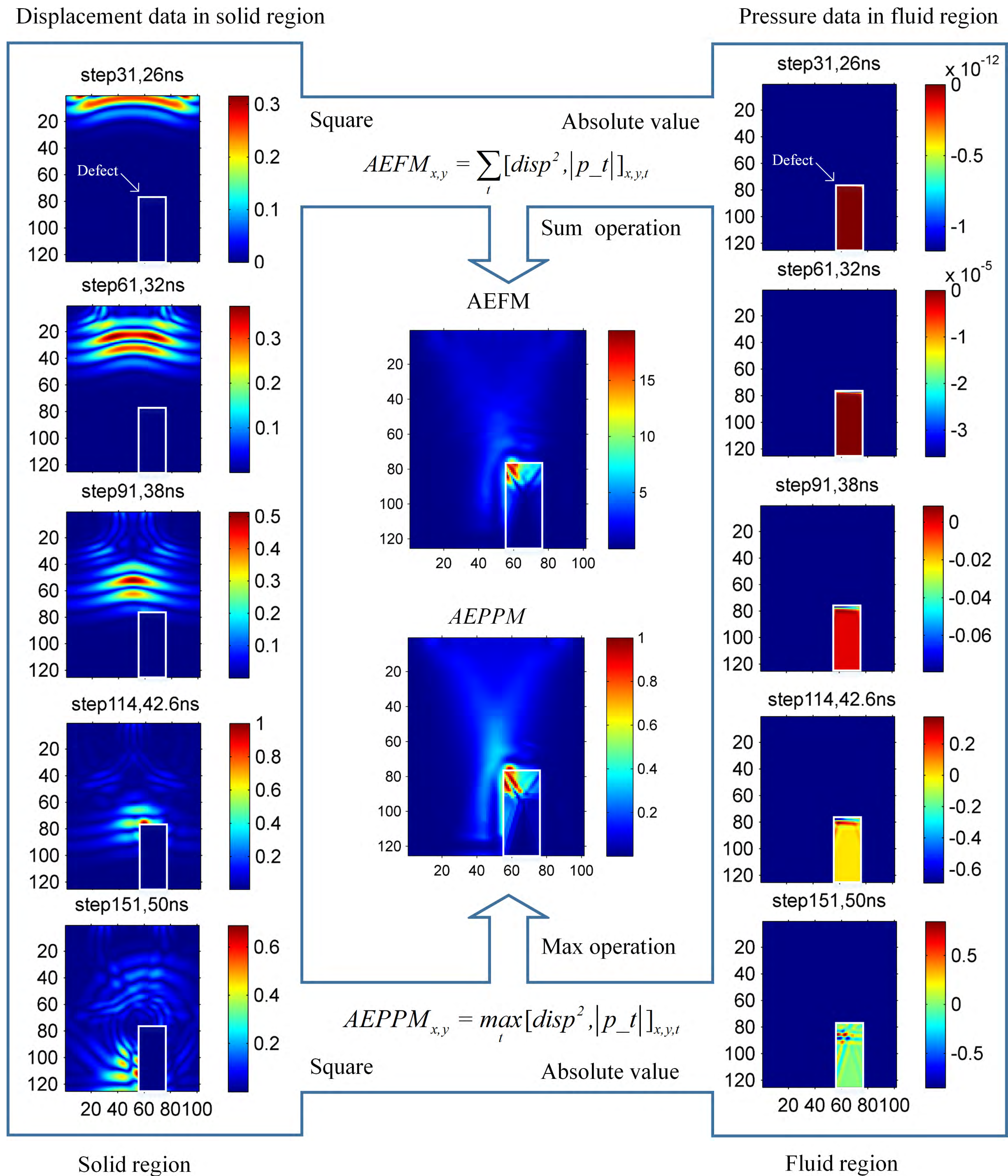

FIGURE 2. The calculation flow diagram of AEFM and AEPPM, taking the microdefect with the width of 20 μm for example (unit in μm, color unit: dB). The figures on both sides are the displacement and pressure sampled from the transient times 26 ns (step 31), 32 ns (step 61), 38 ns (step 94), 42.6 ns (step 114), and 50 ns (step 151), where the white rectangles represent the microdefects.

echo of the microdefect interface, respectively. The peaks of the pulses gradually decrease, which is caused by the energy loss during acoustic reflection in the material interfaces. Since the material is very thin, we used the elastic material model to avoid the acoustic attenuation caused by the material absorption. Thus, the amplitude-frequency spectrums of the pulses have the same central frequency of 234.4 MHz as shown in Figure 3(b), which is close to the central frequency of the physical transducer. Every simulation with different transducer positions produced an A-scan signal. These signals were assembled into a B-scan like image as displayed in Figure 3(c). The position

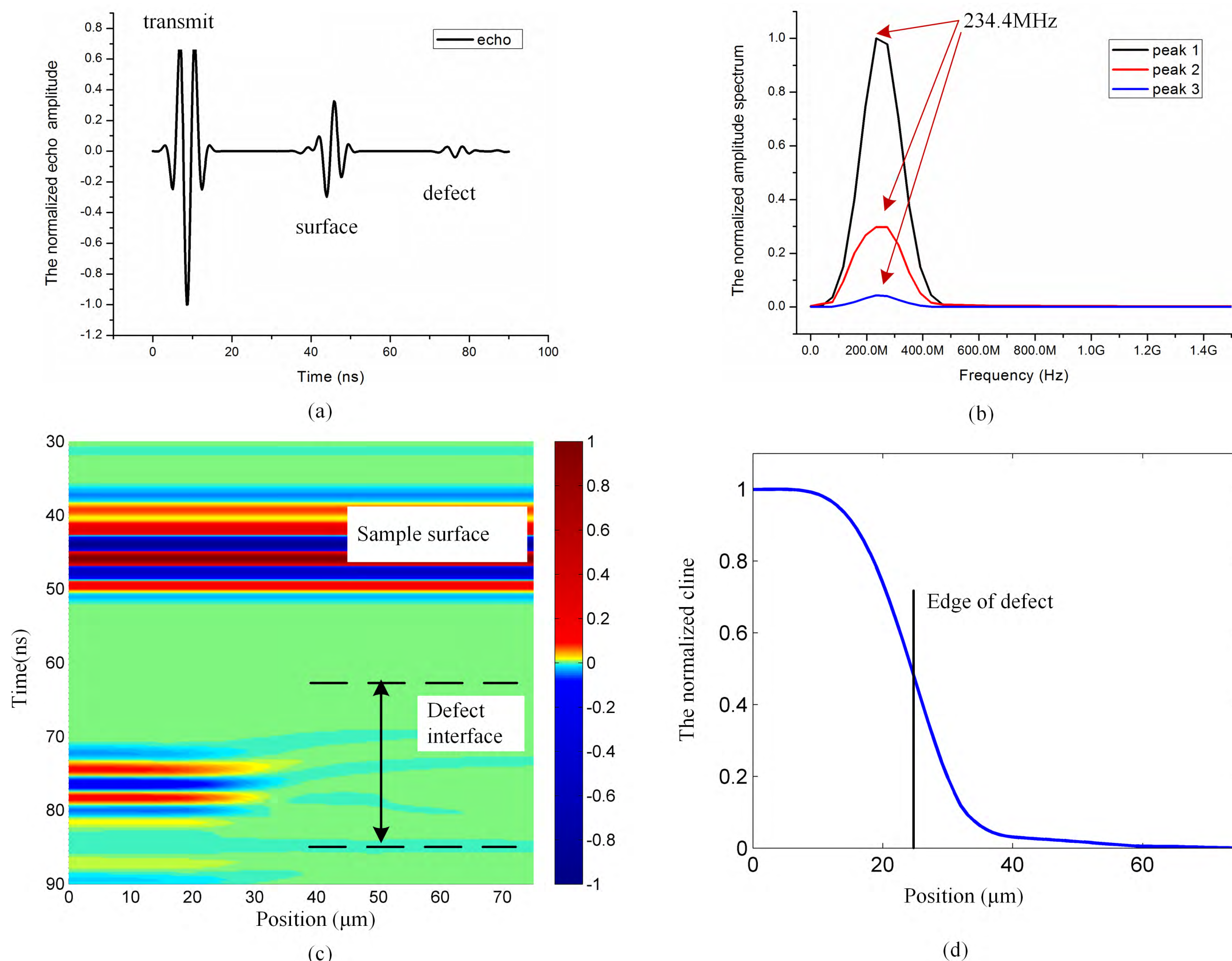

FIGURE 3. The A-scan signal and C-line (unit in μm): (a) normalized A-scan signal; (b) normalized amplitude spectrum of three peaks (color unit: dB); (c) assembled B-scan like image; and (d) C-line obtained from (c).

0 indicates that the transducer is located on the center of the microdefect. The gate denoted by the black dashed lines indicates the echo of the microdefect, which is set from 65 ns to 85 ns. The corresponding value in the C-scan mode can be obtained by calculating the peak echo within the threshold. Normalization of the maximum value of the echo signal of each probe position can get the C-line diagram shown in Figure 3(d). This is the result of the scanning of the microdefect along the line by a probe, named C-line. The C-line decreases when the transducer moves towards the edge of the microdefect.

Figure 4 depicts the C-lines and the corresponding C-scans of the microdefects with the width ranging from 1 μm to 100 μm. When the probe is at the same distance on the left and right sides of the microdefect, the model is bilaterally symmetrical, so the C-line is complemented according to the mirror principle. Obviously, the C-lines for the microdefects larger than the spot all have nearly the same slope together with a platform in different lengths. Here the spot is measured as 27 μm. This makes it easier to effectively extract the microdefect size. If we further reduce the microdefect size, the platform disappears, the maximum value of the C-line decreases, and the slope of the C-line varies with the size. Assuming that the microdefects are circularly symmetrical, corresponding C-scans can be obtained by mapping the C-lines around a central axis as shown in Figure 4(b). In the actual simulation, the microdefects of different sizes had different scan lengths, which means that the size of the C-scan image obtained by the simulation was also inconsistent. When the probe was far away from 0 μm, the value of the C-line was very small and negligible. For better contrast, we removed all the parts of the C-scan image with small values in the edge area, so as to ensure the size of the figure. For those microdefects larger than the spot, the platform shrinks as the size decreases. When the microdefect is further reduced, the intensity of the C-scan will be reduced or even difficult to recognize, making it hard to extract the location and shape.

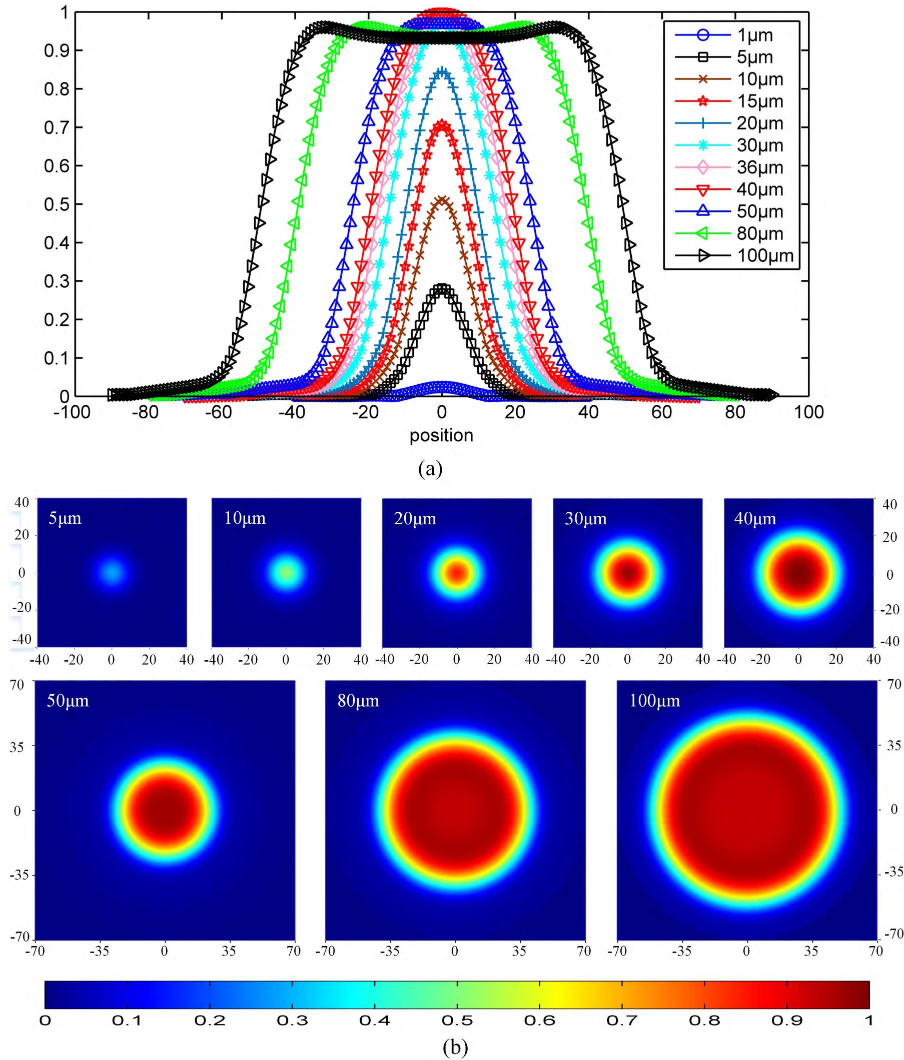

FIGURE 4. The simulated C-lines and the C-scans of the microdefects ranging from 1 μm to 100 μm (unit in μm, color unit: dB): (a) the normalized C-lines; (b) the corresponding C-scans.

C. ACOUSTIC PROPAGATION MAP

AEPPMs are calculated and compared to analyze the energy transmission around the microdefects as shown in Figure 5(a). The left edge of the microdefects is indicated by the red dashed line and is located in the same position referring to the transducer. For example, an edge position of -5 μm means the left edge of the microdefect is located -5 μm to the right of the transducer. The AEPPMs for the microdefects with widths of 10 μm, 20 μm, and 50 μm are obviously different in the edge position -5 μm, as shown in the first column. For the edge position of 5 μm, the AEPPMs especially around the left edge are much more similar, as illustrated in the second column. When the transducer moves to the positions 15 μm and 25 μm, the AEPPMs around the left edge are almost same, as shown in the third and fourth columns. Figure 5(b) depicts the C-lines for the microdefects with the left edge located in the same position. On the position -5 μm, the C-line values for the microdefects with the widths of 10 μm, 20 μm, and 50 μm are different, which is consistent with the first column in Figure 5(a). On the 5 μm position, the C-line values become close for these microdefects, consistent with the second column in Figure 5(a). On the 15 μm and 25 μm positions, the C-line values are almost equal, as shown in the insert. However, the C-line values for the microdefects larger than the spot are nearly equal. Obviously, the edge effects of the C-lines and C-scans are closely related to the acoustic energy transmission around the microdefect.

From the viewpoint of the microdefect size, the acoustic energy peak for the microdefect with a width of 10 μm travels down along the depth direction on both sides of the microdefect when the edge is located at the position of -5 μm or 5 μm, as depicted by the black arrows in the corresponding AEPPMs of Figure 5(a). However, there is just one side for the 50-μm-wide microdefect. This is caused by the microdefects narrower than the spot of the

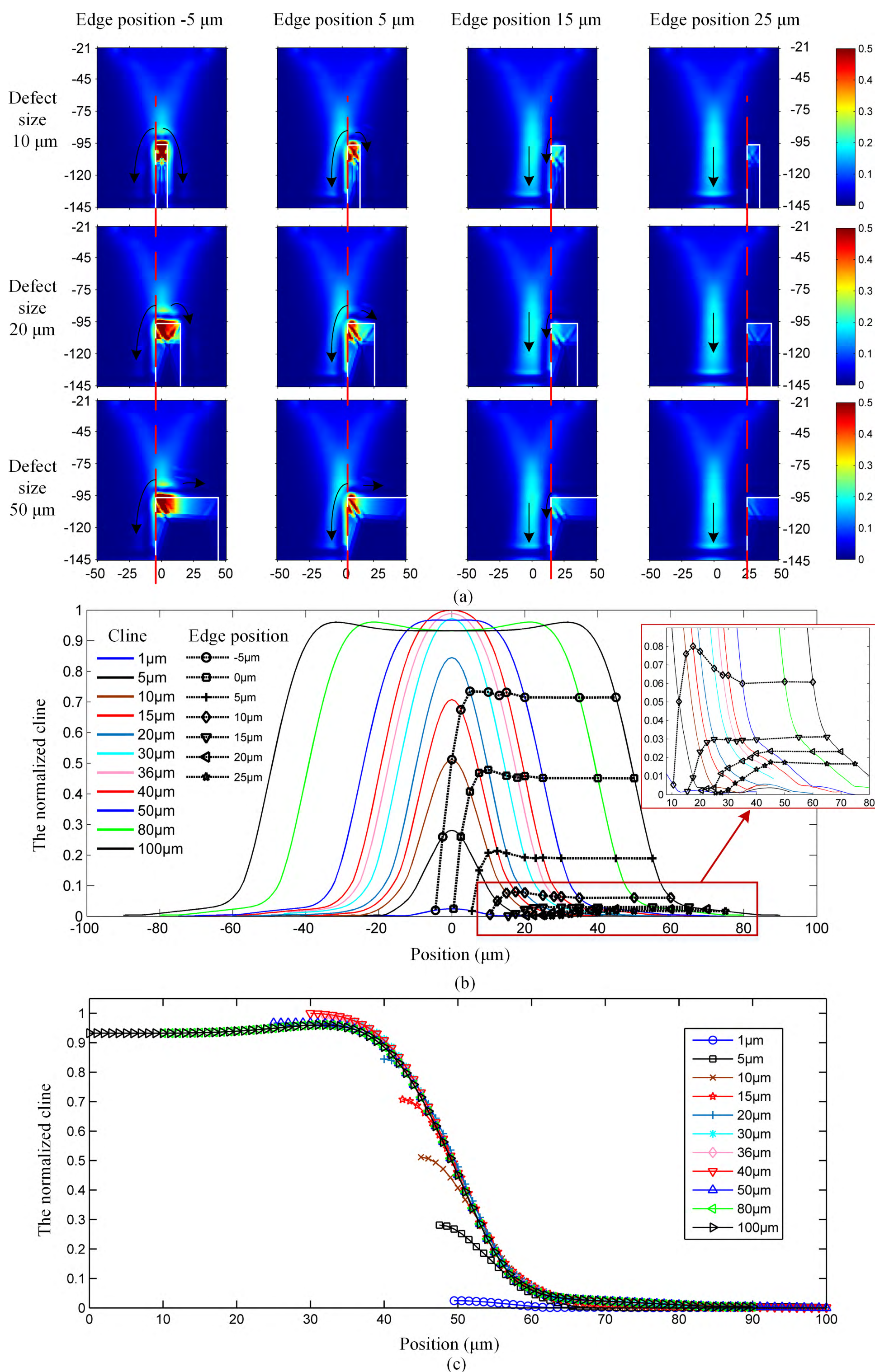

FIGURE 5. The AEPPMs (unit in μm, color unit: dB): (a) the AEPPMs for the microdefects with various widths in different edge positions. From left to right: edges position at -5 μm, 5 μm, 15 μm, and 25 μm. From top to bottom: microdefects with widths of 10 μm, 20 μm, and 50 μm; (b) the C-lines in different edge positions, and (c) shifting all the C-lines together.

acoustic beam. When the edge is far away from the center of the transducer, the acoustic energy peak travels down on only one side for all microdefects, as shown in the AEPPMs for the edge positions of 15 μm and 25 μm. Thus, the C-line data have same slope for the microdefect in more widths when the left edge is further away from the transducer, as shown in the

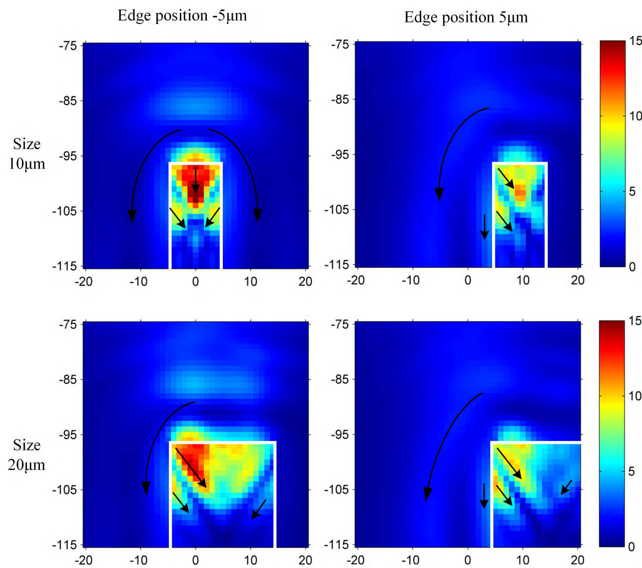

FIGURE 6. Magnified view of the AEFM (unit in μm, color unit: dB). From left to right: the edge positions -5 μm and 5 μm. From top to bottom: the widths of 10 μm and 20 μm.

insert in Figure 5(b). After shifting all the C-lines overlapping together, a basic curve can be observed in Figure 5(c), which is actually the C-lines of the microdefects that are wider than the spot. For the microdefect that is narrower than the spot, a part of the C-line deviates from the basic curve. The smaller the microdefect, the more deviated the part is. The difference between the C-lines is caused by different mechanisms of acoustic energy loss.

Figure 6 shows a magnified view of two defects in two edge positions because the AEFM is roughly similar to the AEPPM. The white lines are the edges of the defects. For the defect with the width of 10 μm and the edge position of -5 μm, the acoustic energy scatters along both sides and refracts into the fluid region from both sides, similar to the AEPPM in Figure 5(a). There is a possibility that the vertical scattering in the solid region is manifested through Lamb waves or surface waves. In the top left of the AEFM, the acoustic energy stacks inside the narrow microdefect, making the energy flux higher than the same region in the case of the other widths, indicated by the deep red region. A similar situation can also be seen in Figure 5(a). Different bands in the fluid region are caused by the interference of the waves originating from different incident sources, showing the same angle with the edge of the microdefect.

III. EXPERIMENTAL VERIFICATION

Because the microdefects in the microparts used in practice are not controllable, it is difficult to obtain a test sample with microdefects, and quantitative analysis cannot be performed. Therefore, we introduced simulated defects in the test samples. Samples with artificial microdefects (the width ranging from 10 μm to 100 μm) were used for verification.

The detailed preparation process was as follows. Firstly, a 4-inch-diameter tungsten wafer was used as the preparation material. After double-sided mechanical polishing, the tungsten sheet has a thickness of 500 $\pm$ 100 μm and a surface roughness Ra of less than 0.1 μm. Theoretical calculations show that when the surface roughness of the sample is less than one-tenth of a wavelength, the improvement in sensitivity is not significant. Here the roughness of the sample surface was less than one-twentieth of the wavelength of the sound wave used, so its effect on sound wave propagation was negligible. Secondly, a layer of aluminum film was deposited on the surface of the metal tungsten by magnetron sputtering as a mask for the subsequent ICP etching step, and the thickness was about 3 μm. Thirdly, the designed pattern was transferred to the aluminum mask by dry etching. The reaction gases were mainly BCl3 and Cl2. The reflection time was about 10 min. Finally, SF6 was used as the main etching gas for metal tungsten; the etching depth was about 50 μm, and the etching time was about 20 min. The wafer was cut into small pieces of about 10 mm $\times$ 10 mm with the cutting machine, as shown in Figure 7(a). The pieces were immersed in water and tested by scanning acoustic microscopy (SAM, D9500, Sonoscan). The scanning range of the microscope in the XY plane is from 1 mm $\times$ 1 mm to 320 mm $\times$ 320 mm, and the scanning axis has a minimum step size of 1 μm. The corresponding image resolution is from 256 $\times$ 256 pixels to 8192 $\times$ 8192 pixels. The 230SP model with a 230 MHz probe has a lens diameter of 1981.2 μm and an underwater focal length of 7924.8 μm. The underwater focus size is 31.8 μm, and the underwater depth of field is 741 μm. The time domain signal sampling frequency is 1 GHz, but there is no function to save the echo signals of all positions in the scanning process, as shown in Figure 7(b). The sampling resolution was 1 μm, which was the same as the step size in the simulation. Finally, the topography of the microdefects was obtained by a laser scanning confocal microscope (LSCM, VK-X200K, Keyence) for comparison.

Figure 7 depicts the experimental results. The sample was measured using an LSCM, and the topography of the artificial microdefect is shown in Figure 7(c), where a profile indicated by the blue arrow is given in Figure 7(d). At a width of 10 μm, the depth of the microdefect is shallow because of the etching process together with the limitations of the LSCM. The C-scan image presented in Figure 7(e) was created by the D9500 device. The scanning probe frequency was 230 MHz, the scanning range was 1600 μm $\times$ 1700 μm, and the scanning step was 2 μm, where a profile indicated by the blue line is shown in Figure 7(f). Because the acoustic impedance of tungsten is much higher than water, only a small amount of energy was reflected by the microdefect, resulting in noisy data that is difficult to analyze. Thus, an average profile along the vertical direction of the region indicated by a red block in Figure 7(e) has been calculated to avoid the interference of noise, which is also shown in Figure 7(f). The C-lines for the microdefects with different widths are extracted from the average profile and shown in Figure 7(g). Similar to the simulation, the slopes of the measured C-lines for large microdefects are almost same. When the

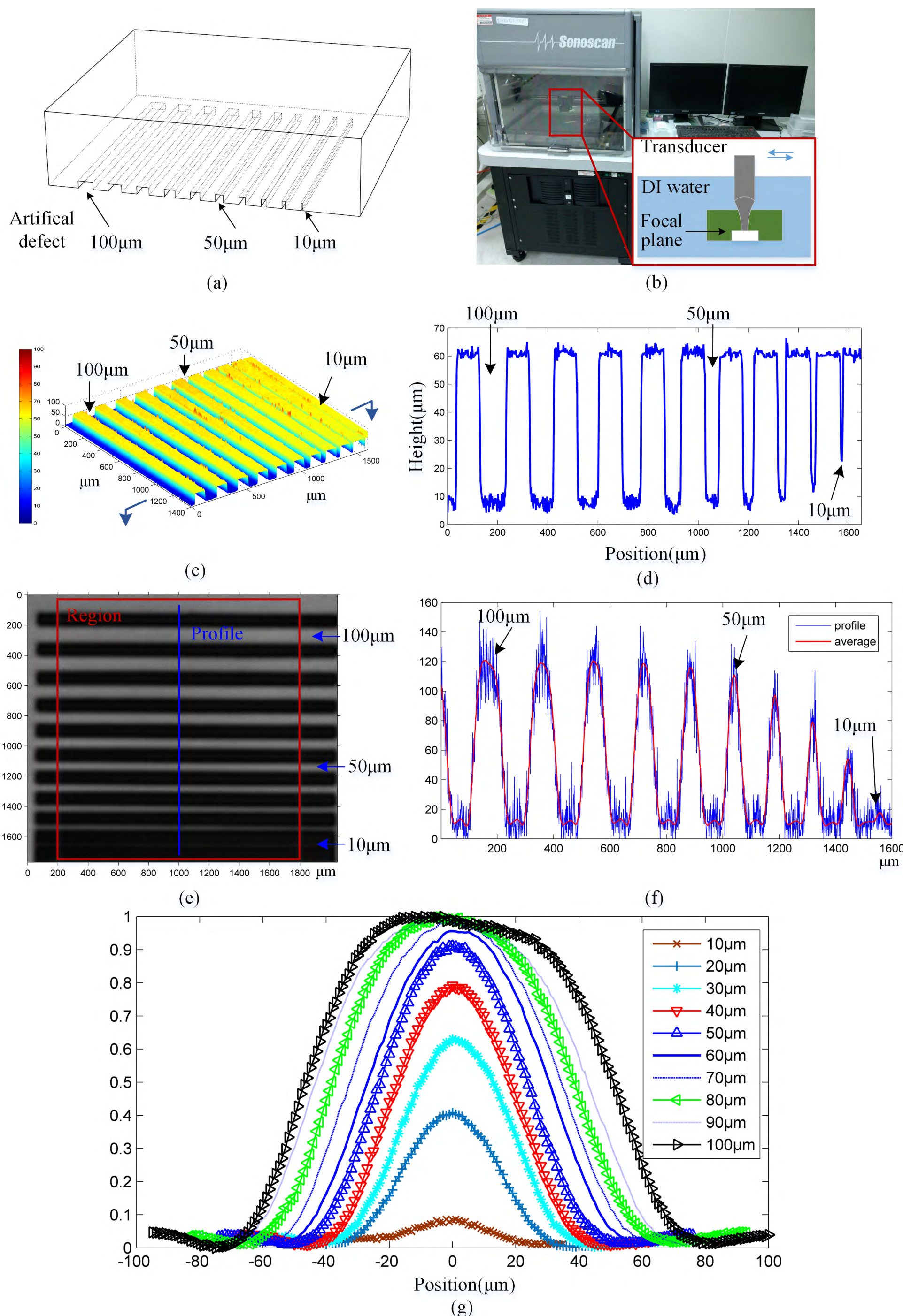

FIGURE 7. Experimental results: (a) the sample; (b) the equipment used in the test. The insert shows the schematic diagram of the AMI; (c) the morphology of the artificial microdefects measured with LSCM; (d) profile indicated by the blue arrow in (c); (e) measured C-scan; (f) profile indicated by the blue line and average profile indicated by the red block in (e); (g) measured C-lines extracted from (f).

width shrinks to about 30 μm, the cap of the C-line disappears. When the width of the microdefects reduces further, the maximum of the C-line decreases and the slope of the C-line changes.

Figure 8 compares the C-lines obtained from experiments against the simulation for different microdefects. The simulation results are generally consistent with the experimental results. From the experimental results, the edge slope of the C-line is smaller than that of the simulation, and the transition zone is wider. This means that the edge of the microdefect will affect the C-line at more probe positions in the experiment. This deviation of the C-line is likely

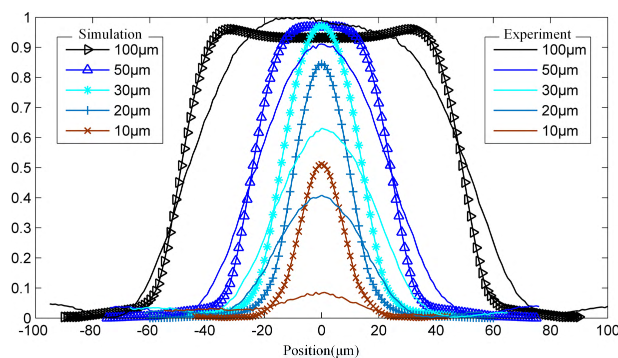

FIGURE 8. **The comparison of the C-lines from experiment and the simulation.**

caused by the sidewall tilt of the microdefect as shown in Figure 7(d).

To effectively detect the shape of the microdefect, the spot size of the transducer should be reduced by increasing the frequency or optimizing the shape of the transducer. Such high-frequency transducers still present problems such as a drastic decrease in the detection depth and high cost. We will study these problems further.

IV. CONCLUSIONS

The performance of microsystems cannot be separated from the reliability of microstructural components, especially when detecting and evaluating microdefects. Microdefects are hidden inside microsystems, and the echo signals of microdefects are weak and susceptible to noise interference, making them particularly difficult to detect.

This paper explored the acoustic interaction behaviors during microdefect detection in acoustic micro-imaging and clarified the edge blurring effects. A transient process simulation model of the high-frequency ultrasonic detection of a microdefect sample was established, and by modifying the position of the virtual probe in the model, the relative position of the probe and the microdefect during the scanning was simulated. The corresponding relationship between the different interfaces and the ultrasonic echo signals was obtained. C-line and C-scan images of different sized microdefects were used to focus on the boundary blurring caused by microdefect edge diffraction during high-precision scanning and its effect on ultrasonic reflection and scattering performance.

The energy reflection and transmission propagation paths of high-frequency pulsed ultrasonic propagation in different sizes of microdefects were different. The changing trend of the C-line was inconsistent, which further leads to different trends in edge blurring in the C-scan image The edge shapes of the C-lines and the C-scans were almost identical for the microdefects larger than the spot, whereas for the microdefects smaller than the spot, the C-lines and the C-scans changed with the size, making it hard to extract the shape of such microdefects. The differences among the C-lines and the C-scans were caused by different energy loss paths around the microdefects. The interaction between the high-frequency pulse, microdefect, and the edge blurring effect in microdefect imaging detection was clarified, which provides a theoretical basis for improving the defect detection accuracy in subsequent research.

Microdefect detection samples were designed and fabricated. The samples were detected by high-frequency ultrasonic scanning with a scanning ultrasonic microscope. The typical microdefect echo signal was obtained. Compared with the simulation results, the edge blurring phenomenon caused by the blurred diffraction of the microdefect edge was proved and they have a good agreement. In the future, this method proposed in this paper shall be studied and applied to IC industrial testing line, so as to improve the accuracy rate of microdefect detection and the yield rate of terminal products.

REFERENCES

[1] A. S. S. Vasan and M. G. Pecht, "Electronic circuit health estimation through kernel learning," *IEEE Trans. Ind. Electron.*, vol. 65, no. 2, pp. 1585–1594, Feb. 2018.

[2] J. Li, L. Han, J. Duan, and J. Zhong, "Interface mechanism of ultrasonic flip chip bonding," *Appl. Phys. Lett.*, vol. 90, no. 24, p. 242902, 2007.

[3] T. I. Shih, Y. C. Lin, J. G. Duh, and T. Hsu, "Electrical characteristics for Sn-Ag-Cu solder bump with Ti/Ni/Cu under-bump metallization after temperature cycling tests," *J. Electron. Mater.*, vol. 35, no. 10, pp. 1773–1780, 2006.

[4] J. Li, W. Wang, Y. Xia, H. He, and W. Zhu, "The soft-landing features of a micro-magnetorheological fluid damper," *Appl. Phys. Lett.*, vol. 106, no. 1, p. 014104, 2015.

[5] L. Su, L. Wang, Ke Li, J. Wu, G. Liao, T. Shi, and T. Lin, "Automated X-ray recognition of solder bump defects based on ensemble-ELM," *Sci. China-Technol. Sci.*, 2018, doi: 10.1007/s11431-018-9324-3.

[6] J. Li *et al.*, "An electromechanical model and simulation for test process of the wafer probe," *IEEE Trans. Ind. Electron.*, vol. 64, no. 1, pp. 1284–1291, Feb. 2017.

[7] F. Wang and F. Wang, "Rapidly Void Detection in TSVs With 2-D X-Ray Imaging and Artificial Neural Networks," *IEEE Trans. Semicond. Manuf.*, vol. 27, no. 2, pp. 246–251, May 2014.

[8] J. Shen, P. Chen, L. Su, T. Shi, Z. Tang, and G. Liao, "X-ray inspection of TSV defects with self-organizing map network and Otsu algorithm," *Microelectron. Rel.*, vol. 67, pp. 129–134, Dec. 2016.

[9] W. Wei, L. Wei, L. Nie, L. Su, and X. Lu, "Using active thermography and modified SVM for intelligent diagnosis of solder bumps," *Infr. Phys. Technol.*, vol. 72, pp. 163–169, Sep. 2015.

[10] X. Lu, T. Shi, J. Han, G. Liao, L. Su, and S. Y. Wang, "Defects inspection of the solder bumps using self reference technology in active thermography," *Infr. Phys. Technol.*, vol. 63, pp. 97–102, Mar. 2014.

[11] L. Su, T. Shi, Z. Liu, H. Zhou, L. Du, and G. Liao, "Nondestructive diagnosis of flip chips based on vibration analysis using PCA-RBF," *Mech. Syst. Signal Process.*, vol. 85, pp. 849–856, Feb. 2017.

[12] L. Zhang, I. C. Ume, J. Gamalski, and K. P. Galuschki, "Study of flip chip solder joint cracks under temperature cycling using a laser ultrasound inspection system," in *Proc. Electron. Compon. Technol. Conf.*, vol. 2, 2009, pp. 1187–1193.

[13] S. Brand *et al.*, "Extending acoustic microscopy for comprehensive failure analysis applications," *J. Mater. Sci., Mater. Electron.*, vol. 22, pp. 1580–1593, Oct. 2011.

[14] G.-M. Zhang, C.-Z. Zhang, and D. M. Harvey, "Sparse signal representation and its applications in ultrasonic NDE," *Ultrasonics*, vol. 52, pp. 351–363, Mar. 2012.

[15] L. Su, T. Shi, Z. Xu, X. Lu, and G. Liao, "Defect inspection of flip chip solder bumps using an ultrasonic transducer," *Sensors*, vol. 13, no. 12, pp. 16281–16291, 2013.

[16] C. S. Lee, G.-M. Zhang, D. M. Harvey, and A. Qi, "Characterization of micro-crack propagation through analysis of edge effect in acoustic microimaging of microelectronic packages," *NDT E Int.*, vol. 79, pp. 1–6, Apr. 2016.

[17] M. Fan, L. Wei, Z. He, W. Wei, and X. Lu, "Defect inspection of solder bumps using the scanning acoustic microscopy and fuzzy SVM algorithm," *Microelectron. Rel.*, vol. 65, pp. 192–197, Oct. 2016.

[18] J. E. Semmens and L. W. Kessler, "Application of acoustic frequency domain imaging for the evaluation of advanced micro electronic packages," *Microelectron. Rel.*, vol. 2, no. 42, pp. 1735–1740, 2002.

[19] S. Brand and F. Altmann, "Lock-in-thermography, photoemission, and time-resolved GHz acoustic microscopy techniques for nondestructive defect localization in TSV," *IEEE Trans. Compon. Packag. Manuf. Technol.*, vol. 8, no. 5, pp. 735–744, May 2018.

[20] J. Zhang *et al.*, "Molecular dynamics simulation of the melting behavior of copper nanorod," *Comput. Mater. Sci.*, vol. 143, pp. 248–254, Feb. 2018.

[21] C. S. Lee, G.-M. Zhang, D. M. Harvey, H.-W. Ma, and D. R. Braden, "Finite element modelling for the investigation of edge effect in acoustic micro imaging of microelectronic packages," *Meas. Sci. Technol.*, vol. 27, no. 2, p. 025601, 2016.

[22] J. W. Ding, V. M. Levin, and Y. S. Petronyuk, "Edge diffraction phenomena in high-resolution acoustical imaging," in *Acoustical Imaging*. Berlin, Germany: Springer, 2012, pp. 299–312.

[23] H. Guochao *et al.*, "Three dimensional acoustical imaging based on iso-surface technique for bulk material," *Sens. Transducers*, vol. 156, no. 9, pp. 168–175, 2013.

LEI SU received the B.S. degree in mechanical engineering from Qingdao University, Qingdao, China, in 2009, and the Ph.D. degree in mechatronic engineering from the Huazhong University of Science and Technology, Wuhan, China, in 2015. He is currently a Lecturer with the College of Mechanical Engineering, Jiangnan University, Wuxi, China. His research interests include signal processing, image processing, and structural health monitoring.

XIAONAN YU received the bachelor's degree in mechanical engineering from Jiangnan University, Wuxi, China, in 2018, where he is currently pursuing the master's degree in mechanical electronics engineering. His research interests include ultrasonic signal processing, image processing, and structural reliability.

KE LI received the B.S. degree in mechanical engineering from Jilin University, Changchun, China, in 1999, and the Ph.D. degree in mechatronic engineering from Mie University, Japan, in 2012. He is currently a Professor with the College of Mechanical Engineering, Jiangnan University, Wuxi, China. His research interests include signal processing, fault diagnosis, and structural health monitoring.

XINGYAN YAO received the B.S. degree in computer science and technology from Hubei University for Nationalities, Hubei, China, in 2007, the M.S. degree in pattern recognition and intelligence systems from the Sichuan University of Science and Engineering, Sichuan, China, in 2010, and the Ph.D. degree in instrument science and technology from Chongqing University, Chongqing, China, in 2014. She is currently an Associate Professor with Chongqing Technology and Business University, Chongqing. Her research interests include prognostic methods on degradation-related machine, smart materials, and vibration control.

MICHAEL PECHT (S'78–M'83–SM'90–F'92) received the B.S. degree in acoustics, the M.S. degrees in electrical engineering and engineering mechanics, and the Ph.D. degree in engineering mechanics from the University of Wisconsin at Madison, Madison, WI, USA, in 1976, 1978, 1979, and 1982, respectively.

He is the Founder of the Center for Advanced Life Cycle Engineering, University of Maryland, College Park, MD, USA, where he is also a Chair Professor. He has been leading a research team in the area of prognostics.

Dr. Pecht is a Professional Engineer and a Fellow of the American Society of Mechanical Engineers. He was a recipient of the IEEE Undergraduate Teaching Award and the International Microelectronics Assembly and Packaging Society William D. Ashman Memorial Achievement Award for his contributions to electronics reliability analysis. He served as the Chief Editor for the IEEE Transactions on Reliability for eight years and an Associate Editor for the IEEE Transactions on Components and Packaging Technology.